# Hole Thermalization Dynamics Facilitate Ultrafast Spatial Charge Separation in CuFeO<sub>2</sub> Solar Photocathodes

Jakub Husek, †,¶ Anthony Cirri, †,¶ Somnath Biswas, † Aravind Asthagiri, ‡ and L. Robert Baker\*, † Department of Chemistry and Biochemistry, The Ohio State University, Columbus, OH 43210 ‡ Department of Chemical and Biomolecular Engineering, The Ohio State University, Columbus, OH 43210, USA

¶ These authors contributed equally
Received May 7, 2018; E-mail: baker.2364@osu.edu

**Abstract:** CuFeO $_2$  is an earth-abundant metal oxide semiconductor showing promising efficiency as a solar photocathode. Using extreme ultraviolet (XUV) and optical spectroscopy we track the element-specific electron and hole dynamics in CuFeO $_2$  and compare results to Fe $_2$ O $_3$ . Cathodic photocurrent, which is only observed in CuFeO $_2$ , is shown to correlate with ultrafast (500 fs) hole thermalization from O 2p to hybridized Cu 3d states, leading to spatial charge separation within the CuFeO $_2$  lattice. These results are supported by DFT calculations confirming strong covalency of Cu 3d and O 2p states at the valence band edge. The ability to elucidate site-specific charge carrier dynamics in real time provides valuable insights for the rational design of catalysts for efficient solar energy harvesting.

#### Introduction

Elucidating the chemical nature and time-dependent evolution of photoexcited states in semiconductor catalysts is critical for understanding the photochemistry of these materials. It is well known that photocatalytic redox activity depends on a number of factors, including band bending at the semiconductor-electrolyte interface, <sup>1</sup> absolute reduction potentials of the band edge, 2 carrier trapping by surface mid-gap states,<sup>3</sup> and distinct surface chemistry on various semiconductor materials. 4 While these effects can be studied using well-established electrochemical methods, it is often more difficult to probe the ultrafast site-specific electron dynamics during photoexcitation and subsequent hot carrier thermalization, trapping, and interfacial charge injection. This difficulty is largely due to a shortage of methods capable of following site-specific electron dynamics on the ultrafast time scale with surface sensitivity and chemical state resolution. Understanding the chemical nature of these excited states is critical for properly modeling the surface photochemistry and interfacial charge transfer dynamics of metal oxides. <sup>5</sup>

Tabletop extreme ultraviolet (XUV) spectroscopy based on high harmonic generation (HHG) can probe element-specific electron dynamics in real-time by showing transient evolution of oxidation states with ultrafast time resolution. To expand this technique to the study of surface electron dynamics in catalytic materials, we have recently developed XUV reflection-absorption spectroscopy.  $^{10-12}$  In this study, we combine XUV reflection-absorption with optical transient absorption and density functional theory (DFT) to provide a detailed picture of charge transfer dynamics in CuFeO<sub>2</sub>, a widely studied photocathode  $^{13-16}$  showing promising efficiency for  $\rm H_2$  evolution  $^{17-19}$  and  $\rm CO_2$ 

reduction.  $^{20-23}$  Results show that irradiation of CuFeO<sub>2</sub> with 400 nm light excites electrons from O 2p valence band to Fe 3d conduction band states, analogous to what has been previously reported for Fe<sub>2</sub>O<sub>3</sub>.  $^{6,11,24}$  Despite identical initial excited states in these two materials, cathodic photocurrent is only observed in CuFeO<sub>2</sub> regardless of applied bias (Figure S3). This study shows that hole thermalization from O 2p to Cu 3d states of CuFeO<sub>2</sub> leads to sub-ps separation of the photoexcited electron and hole within the CuFeO<sub>2</sub> delafossite lattice, which cannot occur in Fe<sub>2</sub>O<sub>3</sub>.

#### **Experimental Section**

All chemicals, preparation, and characterization of materials used in this work are provided in the Supporting Information, along with the photocurrent measurement, XUV probe spectrum, ground state XUV spectra, global fitting, and DFT calculations. Below, details of the experimental procedures for XUV reflection-absorption and optical transient absorption as well as methods for spectral lineshape simulation are provided.

Optical Transient Absorption Spectroscopy. Details of the visible light transient absorption spectrometer and the data analysis are discussed elsewhere, <sup>25</sup> however, specifics pertinent to the experiment carried out in this study will be given. A Ti:sapphire amplifier (Coherent Astrella) produced 8 mJ, 35 fs pulses centered at 800 nm with a 1 kHz frequency. 3 mJ of the fundamental beam are used to pump an optical parametric amplifier to generate the pump pulse, while the white light continuum was generated by focusing 1.5 mJ of the fundamental 800 nm beam into a 1 mm thick CaF<sub>2</sub> plate. The fluorite plate was electronically rotated by 1.5° every 3 s to ensure uniform consistency across the white light spectrum (420 – 700 nm) between generation cycles. All samples were pumped with a 400 nm beam generated by second harmonic generation using the fundamental, focused to a spot size of 7.9 x  $10^{-2}$  mm<sup>2</sup> with an average power of 8 mW. At least three experiments were carried out at random locations on each electrodeposited sample in order to account for synthetic heterogeneity.

Transient XUV Reflection-Absorption Spectroscopy. Details of the experimental setup and processing are described in our previous publications. <sup>10,11</sup> Briefly, a Ti:sapphire amplifier (Spectra-Physics Spitfire Ace), producing 6 mJ, 35 fs pulses centered at 800 nm with a 1 kHz frequency, was used to produce our fundamental light source. The fundamental beam is split between pump and probe beams, with 2 mJ being used to generate the broadband XUV beam by high harmonic generation. Even harmonics are obtained using a symmetry breaking field, whereby 20% of the 800 nm fundamental beam is siphoned from the probe line, and is frequency doubled to 400 nm with a power of 40

 $\mu$ J. After generation of the XUV pulse, an Al foil is used to filter out the visible light driving fields; this filter removes all photon flux above the Al L<sub>1</sub>-edge at 72.6 eV. To generate the pump beam, a separate 800 nm beam is frequency doubled to generate 190 mW of 400 nm light. The size of the XUV beam on the sample at  $8^{\circ}$  incidence angle is 1.01  $\pm$  0.02 mm and 0.137  $\pm$  0.002 mm FWHM in the tangential and sagittal axes, respectively. The pump beam is incident at  $20^{\circ}$  on the sample with an area of 2.43 mm<sup>2</sup>. The sample is raster scanned by 500  $\mu m$  steps in the horizontal and 300  $\mu$ m steps in the vertical direction. Care is taken to collect each data point on a fresh part of the sample. At each point, a set of two spectra are taken: one with both pump and probe beams incident on the sample, and one with only the XUV probe beam, where the latter is used as the reference. The integration time for each spectrum collected at a given spot is 3 s, and the data presented herein, at a given time delay, represent a total of 624 s of integration.

XUV Reflection-Absorption Lineshape Simulation. The details for simulating XUV-RA spectra have been described in depth previously. <sup>10</sup> Briefly, we simulate a ground state absorption spectrum from charge transfer multiplet calculations (CTM4XAS) as developed by de Groot et al. <sup>26,27</sup> Then, from the ground state spectrum we derive the imaginary part of the refractive index using classical electromagnetic theory. Next, the real part of the refractive index is derived via the Kramers–Kronig transformation, and finally, the Fresnel coefficient corrected for non-resonant surface scattering is used to obtain the RA spectrum.

#### Results and Discussion

Figure 1 compares the optical transient absorption kinetics of  ${\rm Fe_2O_3}$  and  ${\rm CuFeO_2}$  upon photoexcitation at 400 nm.  ${\rm Fe_2O_3}$  (Figure 1a) shows a strong excited state absorption (ESA) centered at 580 nm, which has been assigned to transitions of photoexcited electrons in Fe 3d conduction band states. <sup>28</sup> Figure 1b reveals that  ${\rm CuFeO_2}$  shows a similar ESA feature also centered at 580 nm. We likewise assign this feature to conduction band electrons in  ${\rm CuFeO_2}$ . This assignment is supported by XUV spectroscopy and DFT calculations discussed below, which show that conduction band electronic structure and electron localization is very similar in  ${\rm CuFeO_2}$  and  ${\rm Fe_2O_3}$ .

Unlike Fe<sub>2</sub>O<sub>3</sub>, CuFeO<sub>2</sub> also shows a strong ground state bleach (GSB) below 500 nm. A similar GSB has also been reported in Fe<sub>2</sub>O<sub>3</sub>, <sup>28</sup> but the intensity relative to ESA was much lower than we observe in CuFeO<sub>2</sub>. To explain this difference, it should be noted that there are two contributions to a negative feature in a transient absorption measurement: The first is decreased absorption by the material in the excited relative to the ground state, while the second is stimulated emission from the excited state, which will also appear as a GSB. It has been noted that the contribution of valence band transitions is small in Fe<sub>2</sub>O<sub>3</sub> due to the weak transition dipole moment between similar O 2p orbitals composing both the upper valence band and the deeper hole states. <sup>28</sup> In contrast, the upper valence band in CuFeO<sub>2</sub> has significant Cu 3d character as shown both by XUV measurements and DFT calculations discussed below. Because the transition moment between Cu 3d and O 2p states is expected to be greater than for intraband O 2p transitions, the contribution of stimulated emission is also expected to be greater in CuFeO<sub>2</sub> compared to Fe<sub>2</sub>O<sub>3</sub>. This may explain why the GSB is significantly more intense in CuFeO<sub>2</sub> compared to Fe<sub>2</sub>O<sub>3</sub>. Assuming this explanation, the fast recovery of the

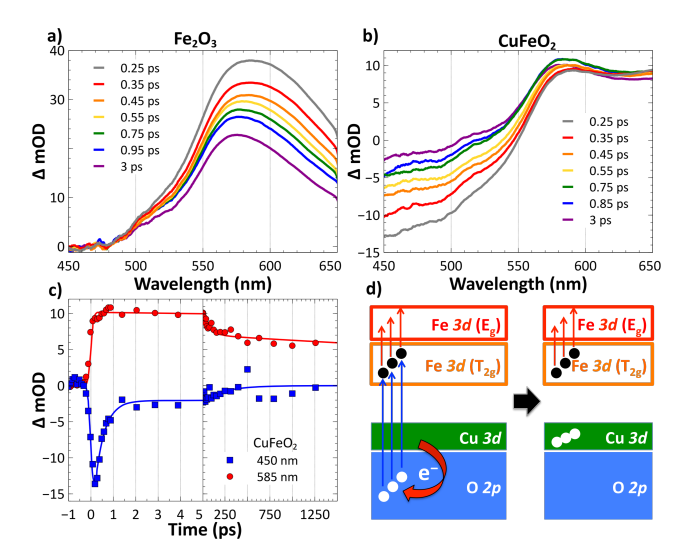


Figure 1. Optical transient absorption kinetics for  $\text{Fe}_2\text{O}_3$  (a) and  $\text{CuFeO}_2$  (b). (c) Kinetic traces of  $\text{CuFeO}_2$  transient spectra showing the time evolution of the GSB (blue) and the ESA (red). (d) Hole thermalization occurs as an electron transfer from the higher lying  $\text{Cu}\ 3d$  states to backfill the photogenerated holes in the lower lying  $\text{O}\ 2p$  states.

GSB corresponds to hole thermalization from O 2p to Cu 3d valence band states, and this conclusion is consistent with element-specific XUV measurements and DFT calculations described below. The fast decay of this feature in  $423\pm34$  fs is also consistent with hot carrier thermalization to band edge. Consequently, hole thermalization in CuFeO<sub>2</sub> can be described as electron transfer from Cu 3d valence band states to backfill holes in deeper O 2p states as depicted in Figure 1d.

Figure 2a and b compare XUV transient reflectionabsorption spectra of Fe<sub>2</sub>O<sub>3</sub> and CuFeO<sub>2</sub>, respectively. As shown in Figure 2a, the transient spectra of photoexcited Fe<sub>2</sub>O<sub>3</sub> are characterized at early times by a ground state bleach centered at 54 eV formed within the 85 fs instrument response function of the XUV spectrometer. This bleach subsequently undergoes a hypsochromic shift to 55.5 eV, and is accompanied by the growth of an excited state absorption feature centered at 52 eV with a correlated time constant of 640 fs. The observed bleach corresponds to the loss of Fe<sup>3+</sup> while the excited state absorption at slightly lower energy is an indication of the formation of Fe<sup>2+</sup>. The fast hypsochromic shift of the GSB bleach feature is the result of lattice expansion during electron self-trapping, and these kinetics have previously been assigned to surface electron trapping and small polaron formation at the catalyst surface. 11

Comparing these results to those obtained for CuFeO<sub>2</sub>, we can divide the spectrum into three regions: 1) the Fe  $\rm M_{2,3}$ -edge ( $3p \to 3d$  transition) centered at  $\sim 54$  eV, 2) the O L<sub>1</sub>-edge ( $2s \to 2p$  transition) extending from 40 to 47 eV, and 3) the Cu  $\rm M_{2,3}$ -edge visible at the high energy side of the spectrum above 63 eV. Nearly identical kinetics are observed at the Fe  $\rm M_{2,3}$ -edge in CuFeO<sub>2</sub> as in Fe<sub>2</sub>O<sub>3</sub> (Figure S6). Furthermore, Figure 2c compares the transient spectrum at the Fe  $\rm M_{2,3}$ -edge obtained at 1 ps for CuFeO<sub>2</sub>, Fe<sub>2</sub>O<sub>3</sub>, and a simulated Fe<sup>2+</sup> charge transfer excited state based on a ligand field multiplet calculation. <sup>11</sup> The excellent match indicates that in CuFeO<sub>2</sub>, photoexcitation results in localization of the excited electron to the Fe 3d conduction band states similar

to Fe $_2$ O $_3$ . A weak ESA feature is also observed in Fe $_2$ O $_3$  at  $\sim \! 44$  eV, corresponding to O L $_1$ -edge absorption by the valence band hole. <sup>12</sup>

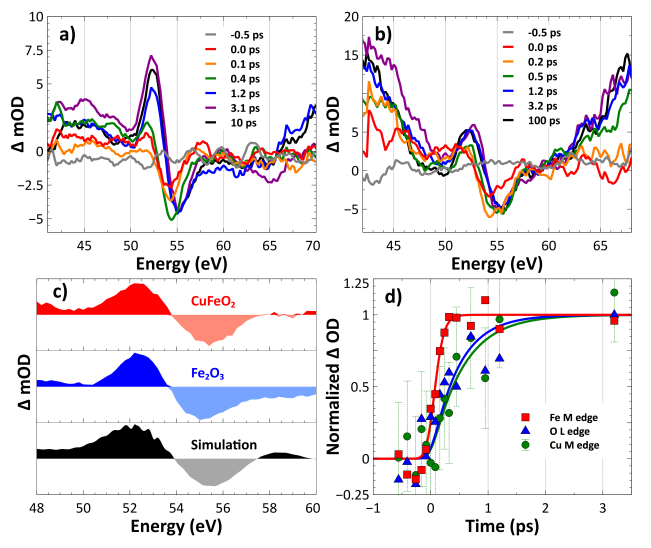


Figure 2. Transient XUV spectra of  $\mathrm{Fe_2O_3}$  (a) and  $\mathrm{CuFeO_2}$  (b) for a series of time delays. (c) Comparison of the XUV transient spectrum at the Fe  $\mathrm{M_{2,3}\text{-}edge}$  obtained 1 ps following photoexcitation for  $\mathrm{CuFeO_2}$  and  $\mathrm{Fe_2O_3}$  along with the result of a ligand field multiplet simulation depicting the expected transient spectrum. (d) Kinetic traces showing the transient response at the Fe  $\mathrm{M_{2,3}\text{-}edge}$ , the Cu  $\mathrm{M_{2,3}\text{-}edge}$ , and the O  $\mathrm{L_{1}\text{-}edge}$ . Traces have been normalized and plotted as positive  $\Delta\mathrm{OD}$  for clarity. Representative standard errors based on replicate measurements are shown for the Cu  $\mathrm{M_{2,3}\text{-}edge}$ .

In contrast to Fe<sub>2</sub>O<sub>3</sub>, CuFeO<sub>2</sub> shows the rise of strong positive absorption extending broadly at the low and high energy regions of the spectrum. This represents strong absorption by the valence band hole at the O L<sub>1</sub> and Cu M<sub>2,3</sub>edges, respectively. Figure 2d shows that the response in these spectral ranges is correlated in time and delayed relative to the signal at the Fe  $M_{2,3}$ -edge. This shows that following an O  $2p \rightarrow \text{Fe } 3d$  charge transfer excitation, hole thermalization to the valence band edge is best described as electron transfer from the higher lying Cu 3d states to backfill holes in the lower lying O 2p states. The effect of these dynamics on the XUV spectra is schematically depicted in Figure 3a. At early times transient signal at the Fe M<sub>2,3</sub>edge reflects electron localization to the Fe 3d conduction band. A weak ESA at the O L<sub>1</sub>-edge shows hole localization to the O 2p valence band. Following hole thermalization strong ESA is observed at the Cu M<sub>2,3</sub>-edge, indicating hole transfer to Cu 3d states. The observed time scales closely match the hole thermalization kinetics observed above using optical transient absorption.

The Cu  $M_{2,3}$ -edge is nominally positioned at 75.1 eV, <sup>29</sup> which is slightly higher than we can access due to a  $\sim$ 70 eV energy cutoff imposed by an Al filter employed in these experiments. Absorption below this cutoff can be understood in terms of strong hybridization of Cu 3d and O 2p states at the valence band edge of this material. Transition metal complexes often display intense rising edge features due to screening induced by charge transfer transitions in the corehole excited state. <sup>30</sup> This has been particularly well studied for the case of Cu complexes, which show that this intense rising edge feature is the result of a two-electron shakedown transition, resulting in increased absorption intensity on the low energy side of the spectrum. <sup>31</sup> Accordingly, this rising

edge has been used as a measure of metal–ligand bond covalency in Cu containing complexes.  $^{32}$  Typical spectral shifts reported at the Cu K-edge are on the order of 5–10 eV,  $^{31}$  consistent with what we measure here. Consequently, the low energy rise of the Cu  $\rm M_{2,3}$ -edge can be understood as the spectral signature of strong Cu–O bond covalency.

Two additional pieces of evidence confirm that this feature is the result of strong covalency of the Cu–O bond. First, the appearance of this feature is correlated with an intense absorption at the O L<sub>1</sub>-edge region of the spectrum, indicating that the thermalized hole is in a delocalized orbital with significant contributions from both Cu 3d and O 2p states. We note that the weak ESA feature that forms initially at the O L<sub>1</sub>-edge in Fe<sub>2</sub>O<sub>3</sub> is also present in CuFeO<sub>2</sub>, consistent with an O 2p  $\rightarrow$  Fe 3d charge transfer excitation. However, this feature is difficult to observe as its growth is convoluted with the delayed formation of the more intense and broader feature resulting from hole thermalization in the hybridized valence band. Second, to quantify the hybridization of Cu and O states, we have performed DFT calculations using the hybrid HSE06 functional <sup>33</sup> with VASP code. <sup>34</sup>

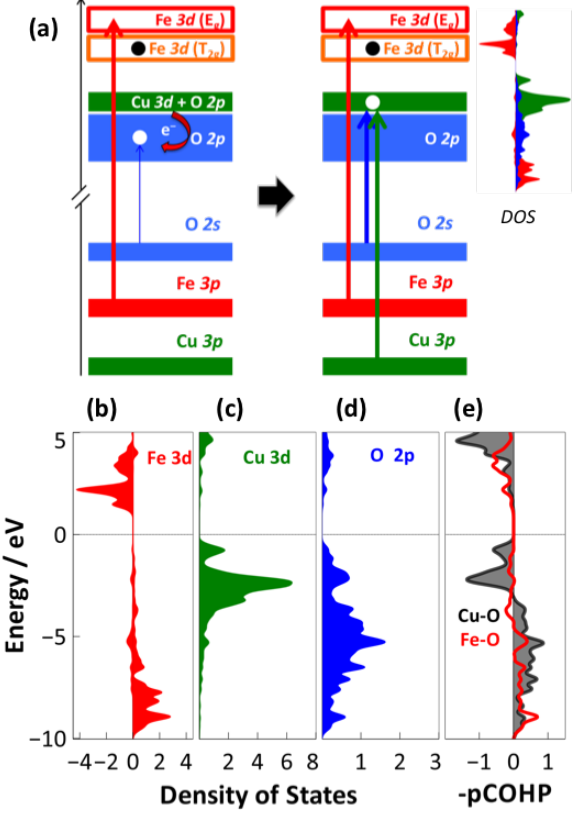


Figure 3. (a) Schematic showing the time evolution of XUV transient reflection-absorption features for an initial O  $2p \rightarrow$  Fe 3d charge transfer excitation followed by hole thermalization to strongly hybridized Cu 3d states at the valence band edge. Projected DOS for (b) Fe 3d, (c) Cu 3d, and (d) O 2p orbitals, respectively. (e) projected COHP between Cu 3d and O 2p states (grey) and between Fe 3d and O 2p states (red). Following convention, -pCOHP is plotted in (d) and a positive (negative) value indicates bonding (antibonding). All energies are relative to the Fermi energy.

DFT HSE06 calculations for CuFeO<sub>2</sub> predict a bandgap of 1.5 eV and a magnetic moment of 4.2  $\mu_B$  on the Fe cation, consistent with reported experimental values of 1.55 eV and 4.2  $\mu_B$  for the band gap and magnetic moment, respectively (Table S1).  $^{35,36}$  Figure 3 plots the projected density of states

pDOS for Fe 3d (b), Cu 3d (c), and O 2p (d) bands in  $CuFeO_2$ . The two Fe 3d bands above the Fermi level are roughly analogous to the  $T_{2g}$  and  $E_g$  states based on crystal field splitting of the Fe 3d orbitals. Figure S7 shows a similar picture for Fe<sub>2</sub>O<sub>3</sub>. To better understand the hybridization between Cu and Fe 3d states with O 2p states, we examine the projected crystal orbital Hamilton population (pCOHP). The COHP measures the overlap between orbitals of pairs of atoms, and indicates bonding, antibonding, and nonbonding contributions between specific atoms. 37 Figure 3e depicts the associated pCOHP between Fe-O and Cu-O orbitals, which reveal particularly strong hybridization between the Cu 3d and O 2p states, including a large antibonding feature from 3 eV to the Fermi level; this covalent Cu-O antibonding orbital represents the valence band maximum. Interestingly, the large antibonding feature would be expected to facilitate hole transfer from the deeper lying O 2p states to the strongly hybridized Cu 3d states in order to reduce antibonding interactions in the photoexcited state of CuFeO<sub>2</sub>. It is further expected that high degree of Cu-O bond covalency at the valence band edge would facilitate the ultrafast transfer of this hole between the strongly coupled electronic states as observed in the ultrafast XUV experiments described above.

### Conclusion

In summary, our work provides important insight for understanding the site-specific electron and hole dynamics in CuFeO<sub>2</sub>. Ultrafast XUV and optical measurements show that photoexcitation leads to charge transfer from O 2p valence band states to Fe 3d conduction band states in both CuFeO<sub>2</sub> and Fe<sub>2</sub>O<sub>3</sub>. Despite similar electron localization in these two materials, different dynamics are observed in both the optical and XUV transient measurements, which arise from the fast relaxation of valence band holes. In CuFeO<sub>2</sub>, carrier thermalization results in fast delocalization of the photoexcited hole to strongly hybridized Cu 3d and O 2p states near the valence band maximum as shown in the pDOS and pCOHP calculations, and we measure a time constant of approximately 500 fs for hole thermalization. In contrast, DFT calculations for Fe<sub>2</sub>O<sub>3</sub> show weak hybridization between Fe 3d and O 2p states near the valence band maximum. The fast hole delocalization observed in CuFeO<sub>2</sub> would tend to weaken the exciton binding energy, which may explain the reason that cathodic photocurrent is observed in this material but not in Fe<sub>2</sub>O<sub>3</sub>. It is important to note that although this study focuses on the early events occurring on the ultrafast time scale in these materials, photoactivity relies on charge transport processes, which span many orders of magnitude in time. The ability of XUV spectroscopy and theory to elucidate site-specific charge carrier thermalization and separation in real time provides a new approach for the rational design of catalysts for efficient solar energy harvesting.

Acknowledgement Preparation and characterization of  ${\rm CuFeO_2}$  photocathodes and XUV spectroscopy of this material were supported by the Air Force Office of Scientific Research under AFOSR award number FA9550-15-1-0204. The DFT work was supported by the National Science Foundation under award number 1665280. We acknowledge the Ohio Supercomputing Center for providing computational resources. We would also like to thank Barbara Dunlap for assistance with optical TA measurements, which were conducted in the Center for Chemical and Biophysical Dynamics at Ohio State University.

Supporting Information Available: Supporting information is available in the online version of the paper. This material is available free of charge via the Internet at http://pubs.acs.org/.

#### References

- Zhang, Z.; Yates Jr, J. T. Band Bending in Semiconductors: Chemical and Physical Consequences at Surfaces and Interfaces. Chem. Rev. 2012, 112, 5520-5551.
- (2) Yang, S.; Prendergast, D.; Neaton, J. B. Tuning Semiconductor Band Edge Energies for Solar Photocatalysis via Surface Ligand Passivation. *Nano Lett.* 2011, 12, 383–388.
- (3) Nagpal, P.; Klimov, V. I. Role of Mid-gap States in Charge Transport and Photoconductivity in Semiconductor Nanocrystal Films. Nat. Commun. 2011, 2, 486.
- (4) Kamat, P. V. Semiconductor Surface Chemistry as Holy Grail in Photocatalysis and Photovoltaics. Acc. Chem. Res. 2017, 50, 527-531
- (5) White, J. L.; Baruch, M. F.; Pander III, J. E.; Hu, Y.; Fortmeyer, I. C. et al. Light-driven Heterogeneous Reduction of Carbon Dioxide: Photocatalysts and Photoelectrodes. *Chem. Rev.* 2015, 115, 12888–12935.
- (6) Carneiro, L. M.; Cushing, S. K.; Liu, C.; Su, Y.; Yang, P. et al. Excitation-wavelength-dependent small polaron trapping of photoexcited carriers in α-Fe<sub>2</sub>O<sub>3</sub>. Nat. Mater. 2017, 16, 819.
- (7) Jiang, C.-M.; Baker, L. R.; Lucas, J. M.; Vura-Weis, J.; Alivisatos, A. P. et al. Characterization of Photo-Induced Charge Transfer and Hot Carrier Relaxation Pathways in Spinel Cobalt Oxide (Co<sub>3</sub>O<sub>4</sub>). J. Phys. Chem. C 2014, 118, 22774– 22784.
- (8) Baker, L. R.; Jiang, C.-M.; Kelly, S. T.; Lucas, J. M.; Vura-Weis, J. et al. Charge Carrier Dynamics of Photoexcited Co<sub>3</sub>O<sub>4</sub> in Methanol: Extending High Harmonic Transient Absorption Spectroscopy to Liquid Environments. Nano Lett. 2014, 14, 5883–5890.
- (9) Vaida, M. E.; Leone, S. R. Femtosecond Extreme Ultraviolet Photoemission Spectroscopy: Observation of Ultrafast Charge Transfer at the n-TiO<sub>2</sub>/p-Si (100) Interface with Controlled TiO<sub>2</sub> Oxygen Vacancies. J. Phys. Chem. C 2016, 120, 2769– 2776.
- (10) Cirri, A.; Husek, J.; Biswas, S.; Baker, L. R. Achieving Surface Sensitivity in Ultrafast XUV Spectroscopy: M<sub>2,3</sub>-Edge ReflectionAbsorption of Transition Metal Oxides. J. Phys. Chem. C 2017, 121, 15861–15869.
- (11) Husek, J.; Cirri, A.; Biswas, S.; Baker, L. R. Surface Electron Dynamics in Hematite (α-Fe<sub>2</sub>O<sub>3</sub>): Correlation Between Ultrafast Surface Electron Trapping and Small Polaron Formation. Chem. Sci. 2017, 8, 8170–8178.
- (12) Biswas, S.; Husek, J.; Londo, S.; Baker, L. R. Highly Localized Charge Transfer Excitons in Metal Oxide Semiconductors. *Nano Lett.* 2018, 18, 1228–1233.
- (13) Prévot, M. S.; Jeanbourquin, X. A.; Bourée, W. S.; Abdi, F.; Friedrich, D. et al. Evaluating Charge Carrier Transport and Surface States in CuFeO<sub>2</sub> Photocathodes. *Chem. Mater.* 2017, 29, 4952–4962.
- (14) Oh, Y.; Yang, W.; Kim, J.; Jeong, S.; Moon, J. Enhanced Photocurrent of Transparent CuFeO<sub>2</sub> Photocathodes by Self-Light-Harvesting Architecture. ACS Appl. Mater. Interfaces 2017, 9, 14078–14087.
- (15) Wuttig, A.; Krizan, J. W.; Gu, J.; Frick, J. J.; Cava, R. J. et al. The Effect of Mg-doping and Cu Nonstoichiometry on the Photoelectrochemical Response of CuFeO<sub>2</sub>. J. Mater. Chem. A 2017, 5, 165–171.
- (16) Prévot, M. S.; Li, Y.; Guijarro, N.; Sivula, K. Improving Charge Collection with Delafossite Photocathodes: A Hostguest CuAlO<sub>2</sub>/CuFeO<sub>2</sub> Approach. J. Mater. Chem. A 2016, 4, 3018–3026.
- (17) Prévot, M. S.; Guijarro, N.; Sivula, K. Enhancing the Performance of a Robust Sol-Gel-Processed p-Type Delafossite CuFeO<sub>2</sub> Photocathode for Solar Water Reduction. *Chem-SusChem* 2015, 8, 1359–1367.
- (18) Jang, Y. J.; Park, Y. B.; Kim, H. E.; Choi, Y. H.; Choi, S. H. et al. Oxygen-Intercalated CuFeO<sub>2</sub> Photocathode Fabricated by Hybrid Microwave Annealing for Efficient Solar Hydrogen Production. Chem. Mater. 2016, 28, 6054-6061.
- (19) Younsi, M.; Aider, A.; Bouguelia, A.; Trari, M. Visible Light-induced Hydrogen over CuFeO<sub>2</sub> via S<sub>2</sub>O<sub>32</sub> Oxidation. Solar Energy 2005, 78, 574–580.
- Energy 2005, 78, 574-580.

  (20) Yang, X.; Fugate, E. A.; Mueanngern, Y.; Baker, L. R. Photoelectrochemical CO<sub>2</sub> Reduction to Acetate on Iron-Copper Oxide Catalysts. ACS Catal. 2016, 7, 177-180.
- (21) Read, C. G.; Park, Y.; Choi, K.-S. Electrochemical Synthesis of P-type CuFeO<sub>2</sub> Electrodes for Use in a Photoelectrochemical Cell. J. Phys. Chem. Lett. 2012, 3, 1872–1876.
- Cell. J. Phys. Chem. Lett. 2012, 3, 1872–1876.

  (22) Gu, J.; Wuttig, A.; Krizan, J. W.; Hu, Y.; Detweiler, Z. M. et al. Mg-Doped CuFeO<sub>2</sub> Photocathodes for Photoelectrochemical Reduction of Carbon Dioxide. J. Phys. Chem. C 2013, 117, 12415–12422.
- (23) Kang, U.; Choi, S. K.; Ham, D. J.; Ji, S. M.; Choi, W. et al. Photosynthesis of Formate from CO<sub>2</sub> and Water at 1% Energy Efficiency via Copper Iron Oxide Catalysis. *Energy Environ*.

- Sci. 2015, 8, 2638-2643.
- (24) Vura-Weis, J.; Jiang, C.-M.; Liu, C.; Gao, H.; Lucas, J. M. et al. Femtosecond M<sub>2,3</sub> Edge Spectroscopy of Transition-Metal Oxides: Photoinduced Oxidation State Change in α-Fe<sub>2</sub>O<sub>3</sub>. J. Phys. Chem. Lett. 2013, 4, 3667–3671.
- Phys. Chem. Lett. 2013, 4, 3667–3671.
  (25) Burdzinski, G.; Hackett, J. C.; Wang, J.; Gustafson, T. L.; Hadad, C. M. et al. Early Events in the Photochemistry of Aryl Azides from Femtosecond UV/Vis Spectroscopy and Quantum Chemical Calculations. J. Am. Chem. Soc. 2006, 128, 13402–13411.
- (26) De Groot, F. Multiplet Effects in X-ray Spectroscopy. Coord. Chem. Rev. 2005, 249, 31–63.
  (27) Stavitski, E.; De Groot, F. M. The CTM4XAS Program for
- (27) Stavitski, E.; De Groot, F. M. The CTM4XAS Program for EELS and XAS Spectral Shape Analysis of Transition Metal L Edges. Micron 2010, 41, 687–694.
- (28) Sorenson, S.; Driscoll, E.; Haghighat, S.; Dawlaty, J. M. Ultrafast Carrier Dynamics in Hematite Films: The Role of Photoexcited Electrons in the Transient Optical Response. J. Phys. Chem. C 2014, 118, 23621–23626.
- Chem. C 2014, 118, 23621–23626.
  Henke, B. L.; Gullikson, E. M.; Davis, J. C. X-ray Interactions: Photoabsorption, Scattering, Transmission, and Reflection at E= 50-30,000 eV, Z= 1-92. At. Data Nucl. Data Tables 1993, 54, 181–342.
- (30) DuBois, J. L.; Mukherjee, P.; Stack, T.; Hedman, B.; Solomon, E. I. et al. A Systematic K-edge X-ray Absorption Spectroscopic Study of Cu (III) Sites. J. Am. Chem. Soc. 2000, 122, 5775-5787.
- (31) Kosugi, N.; Yokoyama, T.; Asakura, K.; Kuroda, H. Polarized Cu K-edge XANES of Square Planar  ${\rm CuCl_4}^{2-}$  ion. Experimental and Theoretical Evidence for Shake-down Phenomena. *Chem. Phys.* **1984**, *91*, 249–256.
- (32) Sarangi, R. X-ray Absorption Near-edge Spectroscopy in Bioinorganic Chemistry: Application to M-O<sub>2</sub> Systems. Coord. Chem. Rev. 2013, 257, 459-472.
- (33) Krukau, A. V.; Vydrov, O. A.; Izmaylov, A. F.; Scuseria, G. E. Influence of the Exchange Screening Parameter on the Performance of Screened Hybrid Functionals. J. Chem. Phys. 2006, 125, 224106.
- (34) Kresse, G.; Hafner, J. Ab Initio Molecular Dynamics for Liquid Metals. Phys. Rev. B 1993, 47, 558.
  (35) Read, C. G.; Park, Y.; Choi, K.-S. Electrochemical Synthesis
- (35) Read, C. G.; Park, Y.; Choi, K.-S. Electrochemical Synthesis of P-type CuFeO<sub>2</sub> Electrodes for Use in a Photoelectrochemical Cell. J. Phys. Chem. Lett. 2012, 3, 1872–1876.
- (36) Ye, F.; Ren, Y.; Huang, Q.; Fernandez-Baca, J. A.; Dai, P. et al. Spontaneous Spin-lattice Coupling in the Geometrically Frustrated Triangular Lattice Antiferromagnet CuFeO<sub>2</sub>. Phys. Rev. B 2006, 73, 220404.
  (37) Dronskowski, R.; Bloechl, P. E. Crystal Orbital Hamilton Pop-
- (37) Dronskowski, R.; Bloechl, P. E. Crystal Orbital Hamilton Populations (COHP): Energy-resolved Visualization of Chemical Bonding in Solids Based on Density-functional Calculations. J. Phys. Chem. 1993, 97, 8617–8624.

## TOC Entry

